

Creation, excitation and ionization of a mesoscopic superatom

T.M. Weber, M. Höning, T. Niederprüm, T. Manthey, O. Thomas,

V. Guarrera¹, M. Fleischhauer, G. Barontini², and H. Ott*

Research Center OPTIMAS, Technische Universität Kaiserslautern, 67663 Kaiserslautern, Germany and

¹ *Present address: LNE-SYRTE, Observatoire de Paris, CNRS,
UPMC, 61 avenue de l'Observatoire, 75014 Paris, France*

² *Present address: Laboratoire Kastler Brossel, ENS,
UPMC-Paris 6, CNRS, 24 rue Lhomond, 75005 Paris, France*

(Dated: December 6, 2024)

Controlling strongly interacting many-body systems enables the creation of tailored quantum matter, with properties surpassing single particle physics. Atomic ensembles which are optically driven to a Rydberg state provide many examples for this, such as atom-atom entanglement [1, 2], many-body Rabi oscillations [3], and strong photon-photon interaction [4]. In its most basic form, Rydberg quantum matter consists of an isolated ensemble of strongly interacting atoms spatially confined to the blockade volume - a so-called superatom. Here, we demonstrate the controlled creation and characterization of an isolated mesoscopic superatom by means of accurate density engineering and excitation to Rydberg p-states. Looking at continuous laser-induced ionization we observe a transition from strongly anti-bunched ion emission under blockade conditions to extremely bunched ion emission under off-resonant excitation. Our experimental setup enables *in vivo* measurements of the superatom, yielding insight into the excitation statistics and dynamics. We anticipate straightforward applications in quantum optics and quantum information as well as future experiments on many-body physics with superatoms.

Rydberg excited superatoms combine single and many-body quantum effects in a unique way and have been proposed as fundamental building blocks for quantum simulation and quantum information [5]. Due to the phenomenon of Rydberg blockade [6] the confined atoms can collectively form an effective two-level system. Changing the extension, the excitation scheme or the driving conditions revives the underlying many-body nature and multiple excitations with pronounced correlations become possible. This tunability and the possibility of multiple usage within a single experimental sequence make superatoms a promising complement to single atom based quantum technology. It is therefore important to understand the significance of the superatom concept and the implications of its finite extension and internal level structure.

The realization of superatom based quantum systems requires the implementation of arbitrary arrangements of isolated mesoscopic atomic ensembles in a scalable way. Here, we prepare an individual superatom by carefully shaping the density distribution of a Bose-Einstein condensate of ^{87}Rb atoms. We first load the condensate in a one dimensional optical lattice with a spacing of 532 nm in order to suppress the axial movement of the atoms. We subsequently compress the atomic sample in the radial direction to reduce its size below the blockade radius and empty all but three (or more) lattice sites using a focussed electron beam [7–9] that is scanned over the sample in consecutive, optimized patterns (Fig. 1a, Methods). The atom number within the remaining atomic ensemble can be adjusted between 100 - 500 at a temperature of $T = (3.5 \pm 0.5) \mu\text{K}$ and its typical size is $\leq 3 \mu\text{m}$ in diameter (Fig. 1b). Our experimental approach is readily scalable to arrays of superatoms (Fig. 1d).

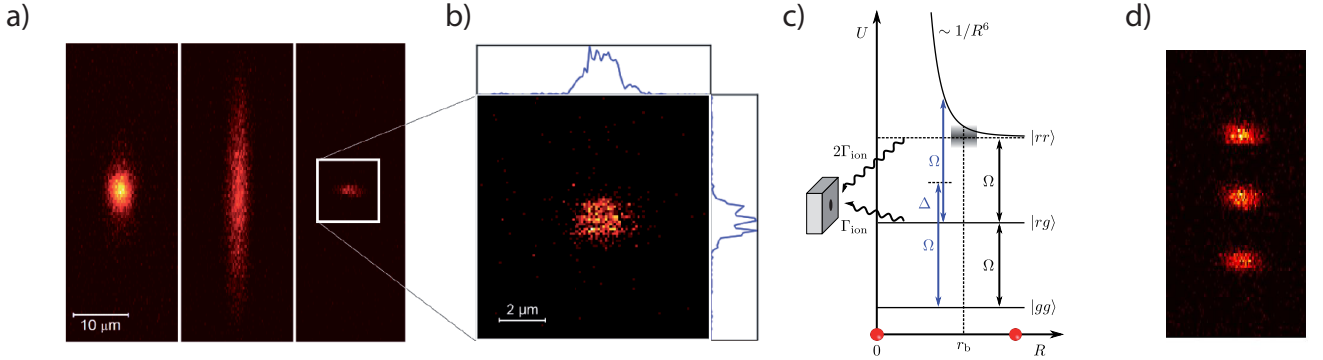


FIG. 1. Preparation of superatoms and excitation level scheme. (a) Starting from a Bose-Einstein condensate in an optical dipole trap with superimposed optical lattice (left) the atoms are radially compressed (middle) and removed from all but a few lattice sites with help of a focused electron beam (right). (b) The resulting almost spherical atomic sample contains between 100 - 500 atoms at a temperature of $3 - 4 \mu\text{K}$ and dimensions smaller than $3 \mu\text{m}$ in each direction. Additionally, the axial size of this atomic sample can be varied arbitrarily. (c) The superatom is excited with a single photon transition ($\lambda = 297 \text{ nm}$) into the $51p$ -state. Effective three-level scheme, comprising the ground state, the singly excited state and the doubly excited state, whose energy has an r^{-6} dependency due to the van-der-Waals interaction. Black (blue) arrows denote (off-)resonant excitation and the blockade radius r_B is denoted by the excitation linewidth (grey shaded area). The decay due to ionization and the ion detection are also indicated. (d) A one-dimensional array of superatoms, demonstrating the scalability of our approach.

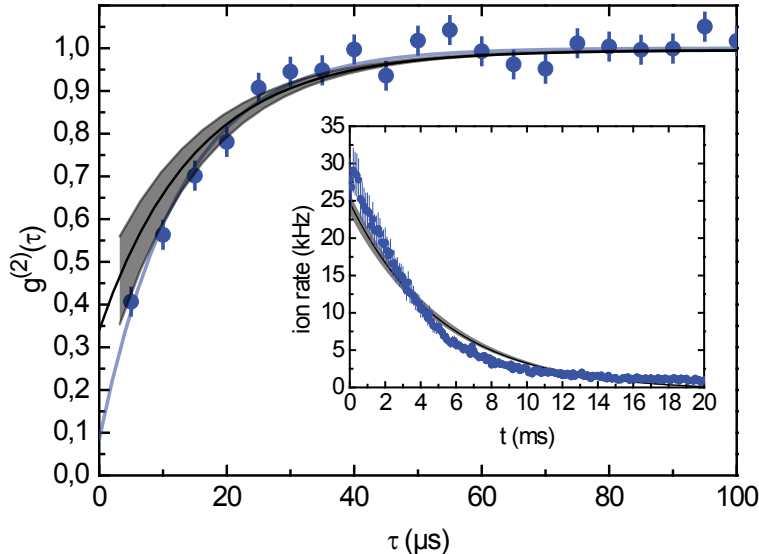


FIG. 2. **Resonant excitation of an isolated superatom.** (a) Second order temporal correlation function of ions emitted from the resonantly excited superatom ($\Omega/2\pi = 6$ kHz)(blue circles). Data points are fitted with an exponential function (blue curve), revealing a value of $g^{(2)}(0) = 0.08 \pm 0.06$. The black line and the grey shaded area results of a rate model (see text). The inset shows the data as well as the fit and model curves of the ion signal as a function of time. The bars denote the statistical errors.

After preparation we excite the atomic ensemble with a single photon transition from the $5S_{1/2}$ -ground state to the $51P_{3/2}, m_j = 3/2$ -Rydberg state at a wavelength of 297 nm. The single photon transition circumvents scattering from any intermediate state and therefore allows for a long-time exposure and, in combination with the superatom concept, for continuous or repeated excitations (and read-outs) of the two-level system in a single experimental run.

Photoionization from the dipole trap laser ($\Gamma_{\text{ion}} = 45 \pm 5$ kHz) is our key mechanism to study the superatom. Upon driving, the superatom emits a string of ions whose statistics are inherited from the Rydberg excitation dynamics. Depending on experimental parameters, it decays on a timescale between a few milliseconds (see inset Fig. 2) and seconds. During this time, almost 100 % of the constituting atoms are converted into ions of which we detect 40 ± 8 %. We evaluate the initial ion rate ($t = 0$) as well as the temporal pair correlation function extracted from the time-resolved ion signal, $g^{(2)}(\tau)$ (Methods).

The blockade conditions within the superatom suppress the excitation of more than one atom for weak resonant driving and the superatom mimics an effective two-level system. As a consequence, the emitted ion string shows explicit anti-bunching (Fig. 2). We extrapolate an initial anti-bunching amplitude $g^{(2)}(0) = 0.08 \pm 0.06$, taking into account an uncorrelated background signal (Methods). This verifies the presence of an efficient blockade within the superatom. As the anti-bunching amplitude stays constant during the decay of the superatom it acts as a continuously operating single ion source [10]. The total suppression of collective oscillations, displayed by the purely exponential shape of $g^{(2)}(\tau)$, denotes that the system is in the overdamped regime, where the intrinsic dephasing mechanisms overcome the coherent coupling.

The ability to experimentally adjust the extension of the atomic sample allows for a continuous transition to a many-body system, where the blockade conditions break down. As multiple excitations are now supported the ion rate rises. In Fig. 3a we show the initial ion rate per atom for increasing axial size l of the sample, keeping the ground state atom density constant. It first decreases under blockade conditions, as more and more atoms contribute to the same signal. Above a critical extension, which we identify with the blockade radius, it remains constant. This indicates the transition to a collection of superatoms. The corresponding anti-bunching signal (inset in Fig. 3a) is a measure of the simultaneous presence of multiple excitations. Both measurements with independent extracted values are compatible with a blockade radius of $2.7 \pm 0.8 \mu\text{m}$. This experimental value allows for the comparison with theoretical models and calculations of the underlying Rydberg interaction physics. On first glance it is quite surprising that we observe a blockade at all as we resonantly excite to a p-state. The corresponding van-der-Waals interaction

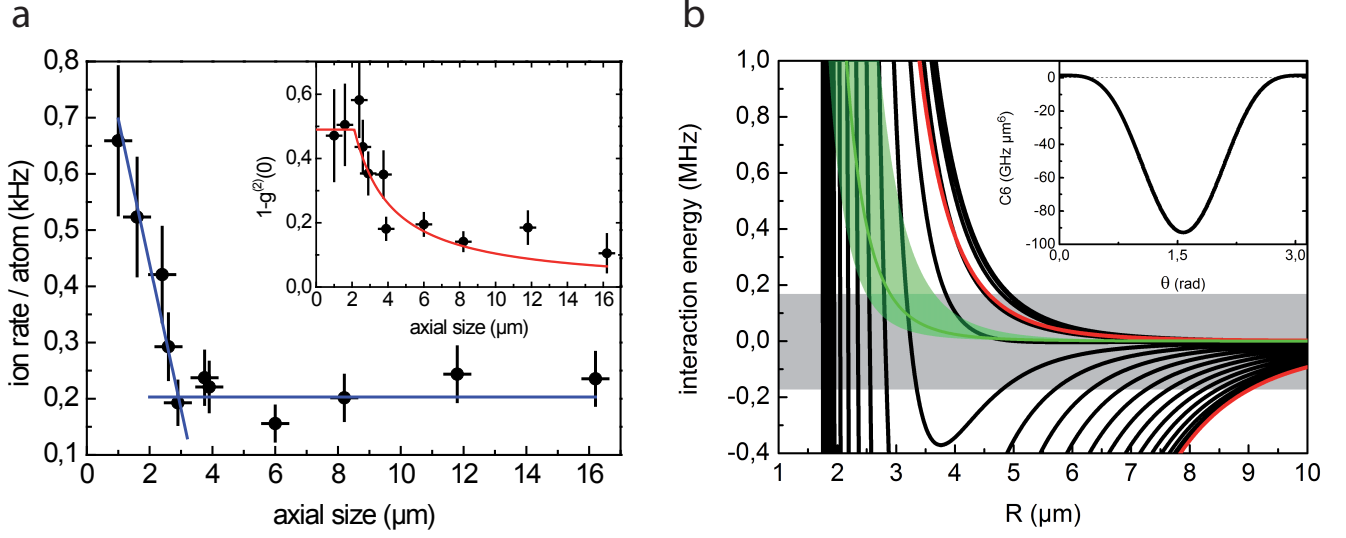


FIG. 3. **Blockade radius measurement and theoretical calculations.** (a) Initially emitted ion rate per atom for different axial sizes l of the atomic sample (black circles). The density is kept constant for all sample sizes. We determine the effective blockade radius from the intersection of partial linear fits (blue curves). The inset shows the corresponding dependence of $g^{(2)}(0)$ on l (black circles). The data are compared to a compound theory (red curve) of a hard shell model (for $l \leq r_B$) and a statistical decay $1 - g^{(2)}(0) = (1 - g_{l < r_B}^{(2)}(0)) \times r_B/l$ (for $l > r_B$). (b) Potential curves of the $51P_{3/2}, m_J = 3/2$ pair state obtained from exact diagonalization of the interaction hamiltonian for equidistant orientation angles from $\theta = 0$ to $\theta = \pi/2$ (black curves). Red curves indicate the C_6 -potentials for $\theta = 0$ and $\theta = \pi/2$. The grey, shaded area denotes the region of resonant excitation for $\gamma = 340$ kHz (Methods). The green curve is the result of the effective rate model with $C_6^{\text{eff}} = 100 \text{ MHz} \times \mu\text{m}^6$, whereas the green shaded area denotes the full range of $40 - 400 \text{ MHz} \times \mu\text{m}^6$. The inset displays the angular dependency of the van-der-Waals coefficient C_6 of the $51P_{3/2}, m_J = 3/2$ state on θ obtained from second order perturbation calculations. The bars indicate the statistical error (ion rate/atom) and the error of the fit for the sample size and the initial $g^{(2)}$ -amplitude.

coefficient C_6 is strongly dependent on the relative orientation of pairs of atoms (see Fig 3b). For a small interval of the orientation angle θ between connecting axis of the two dipoles and quantization axis, C_6 is vanishingly small, potentially leading to a break down of the overall blockade. To understand the underlying interaction physics we need to go beyond the standard C_6 asymptotics. Fig. 3b shows the molecular potential curves for the $51P_{3/2}, m_J = 3/2$ pair state, obtained by exact diagonalization of the interaction Hamiltonian. As a result of an avoided crossing with the $51P_{3/2}, m_J = 1/2$ pair state, which is energetically separated by an external magnetic field, the potential curves which have a negative C_6 coefficient for large distances bend into a repulsive interaction for smaller distances. Thus, the molecular potential curves for all angles become repulsive, enabling an overall blockade.

In order to describe the complex interaction potential structure in an effective but simple way, we assume an isotropic repulsive interaction and solve the many-body problem within an approximate rate equation model with a C_6^{eff} coefficient being the only free parameter (Methods). We chose a van-der-Waals parameter of $100 \text{ MHz} \times \mu\text{m}^6$ in a range of $40 - 400 \text{ MHz} \times \mu\text{m}^6$ to compare it to the experimental results. The model also accounts for internal dephasing and finite laser linewidth. The resulting potential curves are displayed by the green shaded area in Fig. 3b. Throughout this paper, we apply the effective model with these parameters to our data, including the decay and the anti-bunching signal of the superatom (Fig. 2).

Our mesoscopic superatom permits inter-atomic distances of up to $\approx 3 \mu\text{m}$. As a consequence, when the superatom is excited off-resonantly, the blockade conditions can be tuned into an anti-blockade and pronounced bunching of the ion emission can be observed (Fig. 4a). The bunching signal decays exponentially with a time scale given by the lifetime of a Rydberg atom ($\tau = 20 \mu\text{s}$). We find very large bunching values of up to $g^{(2)}(0) = 61 \pm 8$ for large detunings (Fig. 4a). This behaviour can be derived from the full level structure of the mesoscopic superatom including excited states with more than one excitation: while the transition to the first collective Rydberg state is out of resonance, subsequent transitions into doubly excited states are shifted into resonance (Fig. 1c). The increase of bunching with detuning (inset in Fig 4a) is a result of the increasing suppression of single excitations, whereas subsequent and simultaneous pair excitations are facilitated. We observe that up to 15 percent of the ions are produced in pairs, i.e., the time

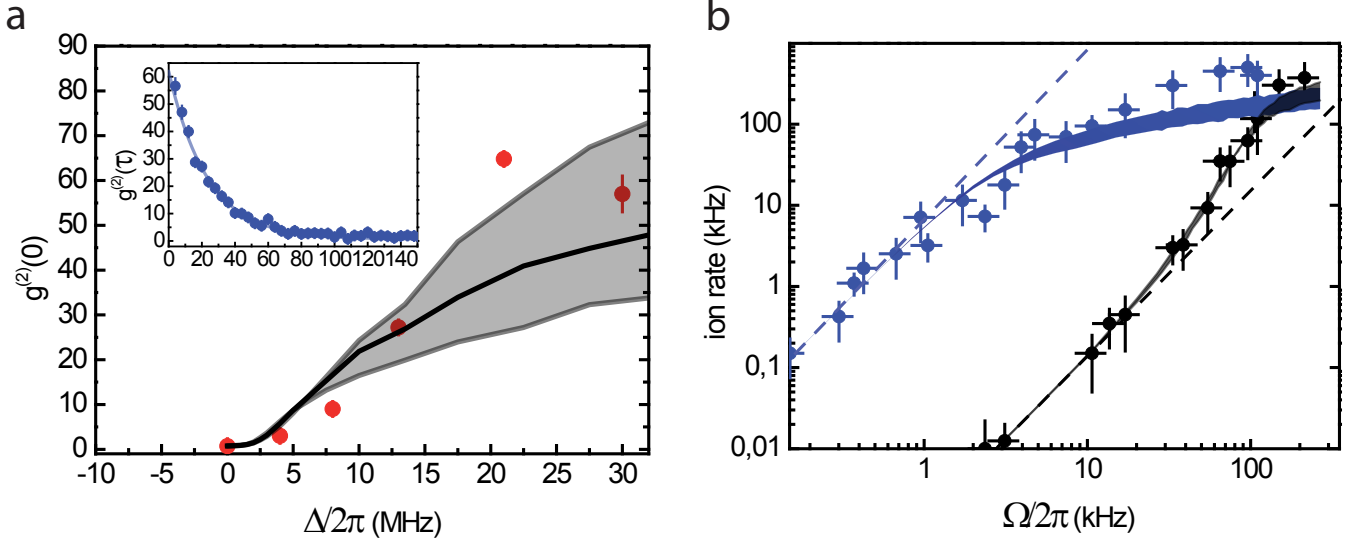


FIG. 4. **Off-resonant excitation and saturation of a mesoscopic superatom** (a) Pair correlation function $g^{(2)}(0)$ for different detuning (red circles, bars indicate the error of the fitted initial amplitude), compared to the model results (grey). Inset: $g^{(2)}(\tau)$ for $\Delta/2\pi = 21$ MHz and $\Omega/2\pi = 48$ kHz (blue circles, bars indicate the statistical error). (b) Dependence of the initial rate of ions emitted from the superatom on the coupling strength $\Omega/2\pi$ for resonant excitation (blue circles) and off-resonant excitation with blue detuning of $\Delta/2\pi = 4$ MHz (black circles) of an ensemble of 125 atoms. Data points are compared to the respective results of the rate model (shaded areas). Dashed lines continue the respective initial quadratic dependence. The vertical bars denote the statistical error, the horizontal bars indicate the intensity fluctuations and drifts of the excitation laser.

interval between two subsequent ions is smaller than the correlation time, while the average time between two events is much larger. Off-resonant excitation statistics have been investigated in bulk systems e.g. via the Mandel-Q factor [11, 12], but the two-particle correlation function of the emitted ions is directly related to the size of the superatom and its characteristic time scale gives a deep insight into the excitation dynamics: the decay constant of $g^{(2)}(\tau)$ denotes the relaxation time for pair state excitations, which equals the lifetime of the Rydberg state for large detunings.

The transition of the mesoscopic superatom from an effective two-level system to a many-level system is also reflected in its saturation behaviour. In Fig. 4b, we plot the initial ion rate in dependence on the Rabi frequency for resonant and off-resonant ($\Delta = 2\pi \times 4$ MHz) excitation together with results from our effective model throughout three orders of magnitude of the experimental parameter Ω . The excitation probability on resonance initially grows quadratically and starts to saturate at an ion rate of 20 kHz, which is about half of the inverse of the lifetime of the Rydberg state - as expected for a two-level system. Driving the superatom stronger, the blockade radius is slightly reduced and above the saturation threshold more excitations fit into the superatom, resulting in an initial ion rate increasing with a smaller slope, determined by boundary conditions. Thus, the blockade is overcome after saturation has been reached. For off-resonant excitation the evolution under strong driving is substantially different. The signal shows again a quadratic initial slope at a reduced absolute value, but enters a region where the slope is steeper than quadratic, showing a strong enhancement of excitations. This is a complementary manifestation of the above described transition to correlated many-particle excitations. For strong enough driving, the resonant and off-resonant excitation eventually reach a comparable level. This happens, when the collective coupling strength $\sqrt{N}\Omega$ becomes comparable with the detuning of 4 MHz and the difference in the first excitation step for the resonant and off-resonant case disappears. As a result, the excitation statistics are determined in both cases by a similar blockade radius.

We have demonstrated the preparation of a single, isolated superatom, which is collectively excited to strongly interacting Rydberg p-states. We have characterized the transition from an effective two-level system to the regime of subsequent pair excitations. Our continuous excitation scheme allows for the long-term investigation of excitation dynamics in both regimes and at their crossover which can be a tool to characterize possible excitation phase transitions [12, 13]. For resonant excitation and even in the far off-resonant regime, where the system is totally determined by its complex level structure, the experimental results are well captured by an effective isotropic rate model.

Single superatoms based on collective Rydberg excitations bear great potential for the study of isotropic and anisotropic long-range interactions and have important applications in quantum optics. They can be used to build high fidelity photon absorbers [14] and deterministic ion sources [10]. An interaction between multiple superatoms can be realized choosing a Förster resonance, which features a long-range r^{-3} dipole-dipole interaction and also enables us to switch to the coherent collective excitation regime, allowing for deterministic state manipulation. Strings of superatoms (see Fig. 1d) are an ideal system for the investigation of energy transfer mechanisms [15, 16] and one-dimensional spin systems [17]. Our approach can be straightforwardly extended to arbitrary patterns of superatoms in two-dimensional lattice systems [7, 8]. Such quantum systems can then be a resource for further investigations of isotropic and anisotropic long-range interactions [18], for the quantum simulation of open spin systems [19, 20], Bell state measurements [21, 22] or interferometric applications [23, 24].

METHODS

Superatom preparation and laser excitation

We start with a Bose-Einstein condensate of about 1700 rubidium atoms in a crossed optical dipole trap at a wavelength of $\lambda = 1064$ nm. The final trap frequencies are $2\pi \times (260/85/270)$ Hz. A one-dimensional optical lattice is then superimposed by linearly ramping up a retro-reflected laser beam along the weak axis of the trap and the axial motion is frozen out. A focused electron beam (250 ± 100 nm radius, 20 nA beam current), which is also used to image the sample, removes the atoms from selected areas [7–9]. In this way, we prepare samples of several hundred atoms with $\leq 3 \mu\text{m}$ diameter at a temperature of $3.5 \pm 1 \mu\text{K}$. After the preparation sequence, a fraction of 10 - 16 % of the atoms dwell in the outer regions of the trap.

The superatom is directly excited to a Rydberg state by illuminating it with an UV-laser beam at 297 nm with a waist of $100 \mu\text{m}$ and laser power up to 160 mW. The light is produced by frequency doubling a stabilized Dye laser (Mattisse-DR) in a heated CLBO-crystal installed in a Pound-Drever-Hall stabilized bow-tie cavity. The frequency of the Dye laser can be tuned via an offset-locked reference laser, resulting in a relative uncertainty of the UV frequency of ± 0.5 MHz. The linewidth of the excitation light is estimated from Dye laser control parameters to less than 200 kHz and the power noise is below 10 %.

Electric fields, ion detection and signal processing

The atomic sample is surrounded by four-segmented copper rings of 40 mm diameter at a distance of 25 mm, embodying an octupole electrodes configuration [25]. Applying corresponding voltages residual electric fields in the chamber are compensated in all directions apart from a remaining permanent vertical component of $E_0 \leq 0.25$ V/cm that is used to extract produced ions towards the ion optics below. The ion optics guide atomic and molecular ions into a dynode multiplier (ETP 14553). The signal pulses are further processed with a temporal resolution of 100 ns.

Temporal correlation function

We numerically calculate the second order temporal correlation function

$$g^{(2)}(\tau) = \frac{\langle I(t)I(t+\tau) \rangle}{\langle I(t) \rangle \langle I(t+\tau) \rangle} \quad (1)$$

where $\langle I(t)I(t+\tau) \rangle$ is calculated as the averaged product of counts (0 or 1) in two bins of distance τ and normalization $\langle I(t) \rangle \langle I(t+\tau) \rangle$ is given by the averaged ion rate. Several effects affect the data evaluation and have to be taken into account. Artefacts from detector ringing occur for time separations of less than 400 ns. Coulomb repulsion between the ions during time of flight produces additional correlations on a timescale which depends on the extraction field. For our parameters, they never occur on timescales longer than $2 \mu\text{s}$. We therefore discard all data points with $\tau \leq 2 \mu\text{s}$. The background atoms (fraction r), contribute an uncorrelated signal to the ion emission of the superatom. This leads to a reduction of the measured amplitude $g_{meas}^{(2)}$ compared to the bare signal from the superatom $g_{real}^{(2)}$ which we correct for: $g_{real}^{(2)}(0) = (g_{meas}^{(2)}(0) - 1)/(1 - r)^2 + 1$.

Effective rate model

The superatom dynamics is described by a Lindblad equation $\dot{\rho} = i(\sum_{j=1}^{N_{\text{atoms}}} [\mathcal{H}_j, \rho] + [\mathcal{H}_{\text{int}}, \rho]) + \sum_{\nu} \frac{1}{2}(2L_{\nu}\rho L_{\nu}^{\dagger} - \{L_{\nu}^{\dagger}L_{\nu}, \rho\})$, where $\mathcal{H}_j = (\frac{\Omega}{2}|r\rangle\langle g|_j + h.c.) + \Delta|r\rangle\langle r|_j$ and L_{ν} are the jump operators for ionization (Γ_{ion}), spontaneous decay into low-lying states which are not ionized (Γ_{sp}) and dephasing (Γ_{d}). The rate of ionization ($\Gamma_{\text{ion}} = 45$ kHz) and internal spontaneous decay ($\Gamma_{\text{sp}} = 5$ kHz) are known from independent measurements and we can extract the dephasing rate from the saturation measurements in Fig. 4b. For weak driving the ion signal is independent of the interaction term \mathcal{H}_{int} and given by $I_{\Omega \ll \gamma} = \frac{\Gamma_{\text{ion}} N_{\text{atoms}}}{\Gamma_{\text{ion}} + \Gamma_{\text{sp}}} \Omega^2 \gamma / (\gamma^2 + 4\Delta^2)$, with $\gamma = \Gamma_{\text{d}} + \Gamma_{\text{ion}} + \Gamma_{\text{sp}}$, and N_{atoms} being the number of atoms within the superatom. Fits to the saturation measurements at $\Delta = 0$ and $\Delta/(2\pi) = 4$ MHz yield the relation between laser intensity and Ω and the decoherence rate $\Gamma_{\text{d}}/(2\pi) \approx 140$ kHz and $\Gamma_{\text{d}}/(2\pi) \approx 340$ kHz, for two different sets of parameters used in the experiment.

Beyond the regime of weak driving we describe the superatom by classical rate equations, which is justified by the large decoherence rate present in our setup and verified in previous studies of strongly interacting Rydberg systems using such methods [11, 26, 27]. Single atom rates for excitation (P_i) and deexcitation (D_i) are determined by the effective detuning $\delta_i = \Delta + \sum_j \frac{C_6^{\text{eff}}}{|r_i - r_j|^6} |r\rangle\langle r|_j$ through $P_i = \frac{\Omega^2 \gamma}{4\delta_i^2 + \gamma^2}$ and $D_i = \frac{\Omega^2 \gamma}{4\delta_i^2 + \gamma^2} + \Gamma_{\text{ion}} + \Gamma_{\text{sp}}$. The set of many body rate equations is solved by stochastic sampling of trajectories. Simulations take into account the spatial distribution of atoms as measured in the experiment by averaging over many realizations. Atomic motion is not included within our description and the intricate p-state interaction is approximated with an effective, isotropic van der Waals potential C_6^{eff}/r^6 .

* ott@physik.uni-kl.de

- [1] Gaëtan, A. *et al.* Observation of collective excitation of two individual atoms in the Rydberg blockade regime. *Nature Phys.* **5**, 115-118 (2009).
- [2] Urban, E. *et al.* Observation of Rydberg blockade between two atoms. *Nature Phys.* **5**, 110-114 (2009).
- [3] Dudin, Y. O., Li, L., Bariani, F. & Kuzmich, A. Observation of coherent many-body Rabi oscillations. *Nature Phys.* **8**, 790-794 (2012).
- [4] Peyronel, T. *et al.* Quantum nonlinear optics with single photons enabled by strongly interacting atoms. *Nature* **488**, 57-60 (2012).
- [5] Saffman, M., Walker, T. G. & Mølmer, K. Quantum information with Rydberg atoms. *Rev. Mod. Phys.* **82**, 2313-2363 (2010).
- [6] Lukin, M. D. *et al.* Dipole Blockade and Quantum Information Processing in Mesoscopic Atomic Ensembles. *Phys. Rev. Lett.* **87**, 037901 (2001).
- [7] Gericke, T., Würtz, P., Reitz, D., Langen, T. & Ott, H. High-resolution scanning electron microscopy of an ultracold quantum gas. *Nat. Phys.* **4**, 949-953 (2008).
- [8] Würtz, P., Langen, T., Gericke, T., Koglbauer, A. & Ott, H. Experimental Demonstration of Single-Site Addressability in a Two-Dimensional Optical Lattice. *Phys. Rev. Lett.* **103**, 080404 (2009).
- [9] Barontini, G., Labouvie, R., Stubenrauch, F., Vogler, A., Guarrera, V. & Ott, H. Controlling the Dynamics of an Open Many-Body Quantum System with Localized Dissipation. *Phys. Rev. Lett.* **110**, 035302 (2013).
- [10] Ates, C., Lesanovsky, I., Adams, C. S. & Weatherill, K. J. Fast and Quasideterministic Single Ion Source from a Dipole-Blockaded Atomic Ensemble. *Phys. Rev. Lett.* **110** 213003 (2013).
- [11] Schempp, H., Whitlock, S., Weidemüller, M. *et al.* Full Counting Statistics of Laser Excited Rydberg Aggregates in a One-Dimensional Geometry. *Phys. Rev. Lett.* **112**, 013002 (2014).
- [12] Malossi, N. *et al.* Full counting statistics and phase diagram of a dissipative Rydberg gas. *Phys. Rev. Lett.* **113** 023006 (2014).
- [13] Carr, C., Ritter, R., Wade, C. G., Adams, C. S. & Weatherill, K. J. Nonequilibrium Phase Transition in a Dilute Rydberg Ensemble. *Phys. Rev. Lett.* **111** 113901 (2013).
- [14] Honer, J., Löw, P., Weimer, H., Pfau, T. & Büchler, H. P. Artificial Atoms Can Do More Than Atoms: Deterministic Single Photon Subtraction from Arbitrary Light Fields. *Phys. Rev. Lett.* **107**, 093601 (2011).
- [15] Westermann, S. *et al.* Dynamics of resonant energy transfer in a cold Rydberg gas. *Eur. Phys. J. D* **40**, 37-43 (2006).
- [16] Wüster, S., Ates, C., Eisfeld, A. & Rost, J. M. Excitation transport through Rydberg dressing. *New J. Phys.* **13**, 073044 (2011).
- [17] Lesanovsky, I. Liquid Ground State, Gap, and Excited States of a Strongly Correlated Spin Chain. *Phys. Rev. Lett.* **108**, 105301 (2012).
- [18] Glaetzle, A. W., Dalmonte, M., Nath, R., Rouschatzakis, I., Moessner, R., & Zoller, P. Quantum Spin Ice and dimer models with Rydberg atoms. *arXiv:1404.5326*.
- [19] Höning, M., Muth, D., Petrosyan, D. & Fleischhauer, M. Steady-state crystallization of Rydberg excitations in an optically driven lattice gas. *Phys. Rev. A* **87**, 023401 (2013).

- [20] Höning, M., Abdussalam, W., Fleischhauer, M., & Pohl, T. Antiferromagnetic long-range order in dissipative Rydberg lattices. *arXiv:1404.1281*.
- [21] Möbius, S., Genkin, M., Eisfeld, A., Wüster, S. & Rost, J. M. Entangling distant atom clouds through Rydberg dressing. *Phys. Rev. A* **87**, 051602 (2013).
- [22] Wüster, S., Möbius, S., Genkin, M., Eisfeld, A. & Rost, J. M. Source of entangled atom pairs on demand, using the Rydberg blockade. *arXiv:1309.7307*. (2013).
- [23] Ran Wei, R., Zhao, B., Deng, Y., Chen, Y.-A. & Pan, J.-W. Deterministic spin-wave interferometer based on the Rydberg blockade. *Phys. Rev. A* **83**, 063623 (2011).
- [24] Gil, L. I. R., Mukherjee, R., Bridge, E. M., Jones, M. P. A., & Pohl, T. Spin Squeezing in a Rydberg Lattice Clock. *Phys. Rev. Lett.* **112**, 103601 (2014).
- [25] Manthey, T., Weber, T. M., Niederprüm, T., Langer, P., Guarrera, V., Barontini, G. & Ott, H. Scanning electron microscopy of Rydberg-excited Bose-Einstein condensates. *arXiv:1403.1761*.
- [26] Ates, C., Pohl, T., Pattard, T. & Rost, J. Strong interaction effects on the atom counting statistics of ultracold Rydberg gases. *J. Phys. B: At. Mol. Opt. Phys.* **39**, L233 (2006).
- [27] Petrosyan, D., Höning, M. & Fleischhauer, M. Spatial correlations of Rydberg excitations in optically driven atomic ensembles. *Phys. Rev. A* **87**, 053414 (2013).

Acknowledgements

We acknowledge financial support by the DFG within the SFB/TRR 49. V. G. and G. B. were supported by Marie Curie Intra-European Fellowships.

Author Contributions

T. W., T. M., T. N., G. B., and H. O. designed and set up the apparatus. G.B. and H. O. conceived the experiment. T. W., T. N., O. T., T. M., and G. B. performed the experiment. H. O. supervised the experiment. T. W. analyzed the data and prepared the manuscript. M. H. and M.F. developed the theoretical model. M. H. made the numerical simulations. M. F. supervised the numerical simulations. All authors contributed to the data interpretation and manuscript preparation.